Stability of plane Couette flow with constant wall transpiration

W. Sun and A. Yalcin

Chair of Fluid Dynamics, TU Darmstadt, Otto-Berndt-Straße 2, 64287 Darmstadt, Germany

M. Oberlack [*]

Chair of Fluid Dynamics, TU Darmstadt, Otto-Berndt-Straße 2, 64287 Darmstadt, Germany
and Centre of Computational Engineering, TU Darmstadt, Dolivostraße 15, 64293 Darmstadt, Germany

Plane Couette flow with constant wall transpiration, i.e., constant blowing from below and constant suction from above, is a solution of the Navier-Stokes equations in terms of exponentials. It is characterized by two Reynolds numbers Re and Re_V, where Re parametrizes the moving wall and Re_V describes the influence of the transpiration. For this flow the modified Orr-Sommerfeld equation admits one of the very few exact solutions in terms of hypergeometric functions. Based on this, we solve the stability problem, though for the main part focus on temporal stability. For small wall-transpiration rates up to $\mathrm{Re}_V \simeq 6.71$, the flow remains unconditionally stable, analogous to the classical Couette flow for arbitrary Reynolds numbers Re. By further increasing Re_V an instability sets in and a minimum critical Reynolds number of Re = 668 350.491 is reached at $\mathrm{Re}_V = 9.799$. Hence, around this point, the destabilizing effect of blowing outweighs the stabilizing effect of suction. By further increasing the transpiration rate beyond this point, the corresponding critical Reynolds number Re increases again and continues to grow. This limiting case is accompanied by the development of a strong boundary-layer-like velocity profile near the upper wall and the flow transitions to the asymptotic suction boundary layer (ASBL). Thus, the present analysis comprises the whole range from classical Couette flows extended by transpiration to the ASBL, which is known to have a strongly stabilizing effect.

I. INTRODUCTION

One of the most classical methods of laminar flow control is to apply suction or blowing at the wall. Early experimental studies of suction for the control of the laminar boundary layer demonstrated that boundary-layer transition can be delayed by suction of the near-wall flow. References [1,2] used a wing whose surfaces contained many thin and closely spaced spanwise suction slits to demonstrate the decrease in drag associated with delayed transition. The theoretical treatment of constant suction to boundary-layer flows is considerably simplified by assuming continuous suction through a flat plate. The stabilizing effect of constant suction to boundary-layer flows was first theoretically studied for the inviscid case in [3], which indicated that the amplification rate of unstable disturbances for the asymptotic profile is an order of magnitude less than that for the

---

[*]oberlack@fdy.tu-darmstadt.de

Blasius boundary layer. Only a few years later those results were reviewed and extended in [4]. In particular, that work showed that with an asymptotic suction profile the inviscid form of the Orr-Sommerfeld equation (OSE) can be transformed into a hypergeometric equation and thus solved exactly. Reference [5] derived an analytical solution for the simplified inviscid case composed of Gaussian hypergeometric functions. For the viscous case, the stability of this flow was numerically analyzed in [6]. Therein it was pointed out that suction applied at the wall is an effective method to delay the laminar-turbulent transition. The critical Reynolds number for the asymptotic suction boundary layer (ASBL) was given as $\mathrm{Re} = 54\,370$, later corrected to $\mathrm{Re} = 54\,382$ in [7], which employed Chebyshev collocation methods, and recently further refined to $\mathrm{Re} = 54\,378$ in [8], which solved the OSE analytically.

Additionally, the linear stability analysis (LSA) of various combinations of channel and Couette flow with crossflow have a long history. Reference [9] investigated the influence of a constant crossflow through porous channel walls on the stability of plane Poiseuille flow numerically using the Galerkin method. That work demonstrated that the crossflow has a stabilizing effect, leading to an increase in the critical Reynolds number with increasing crossflow velocity. In addition to plane Poiseuille flow, the studies on the hydrodynamic stability of plane Couette flow (PCF) have also received considerable attention. However, the linear stability analysis of PCF showed that the flow is linearly stable (see Ref. [10]) for all Reynolds numbers. Nevertheless, it has been observed in experiments that PCF undergoes transition at a Reynolds number as low as 360 ± 10 (see Ref. [11]). Reference [12] conducted a numerical and asymptotic study on the LSA of parallel wall-bounded flows with injection at the lower wall and suction at the upper wall. Notably, that investigation considered a very special form of flow, which consists of a combination of Couette, Poiseuille and wall-transpiration flows. The analytical solution therein depends on the dimensionless pressure gradient parameter Π, and only when this parameter is set to $\Pi = 0$, the base flow matches our base flow of the plane Couette flow with constant wall transpiration (PCFT). However, in that study, the pressure gradient parameter Π was set to $\Pi = \mathrm{Re}_V/\mathrm{Re}$, where the Reynolds numbers Re_V and Re are based on the injection velocity V_0 and the upper wall velocity U_w, respectively. With this, the base flow becomes linear and the boundary-layer type of behavior disappears, which is quite different from our base flow. In conclusion, Ref. [12] covers only a very narrow range of parameters from the aforementioned flows. In contrast, the present work focuses on the combination of the Couette flow with wall transpiration and covers the entire parameter range of these two flows. Still, in the study in [12] it was shown that due to the injection process, the eigenmodes are significantly reorganized in the complex plane, resulting in the linear instability of certain modes. That work determined numerically a critical injection Reynolds number $\mathrm{Re}_V \simeq 48$ for streamwise Reynolds numbers of $\mathrm{Re} > 3300$. The study also found that higher injection rates stabilize the flow.

The study conducted in [13] employed a numerical investigation using a spectral-element code to examine the impact of a spanwise-oriented ribbon on the stability of PCF. In that investigation, PCF was perturbed by the presence of a wire positioned midway between the bounding plates and oriented in the spanwise direction. The investigation aimed to understand how a minor geometric perturbation of the plane Couette geometry influences flow stability. It modeled the ribbon by no-slip boundary condition in the simulation therein and computed two-dimensional (2D) steady solutions of the Navier-Stokes equations for the perturbed configuration and carried out the linear stability analysis of these solutions. It was found that the 2D steady flow loses stability at $\mathrm{Re} \simeq 230$ for a nondimensional height of the ribbon of $\rho = 0.086$. Reference [14] probably was the first detailed instability exploration of the PCFT, i.e., exactly the flow that we investigate presently. The main aim therein was to compare the high-Re energy dissipation rate to an upper bound. Interesting enough, it was found that this flow is an example of steady laminar flows in which the dissipation is finite in the zero-viscosity limit, if at least a small amount of transpiration is present. For the further analysis both energy stability and classical LSA were emplyed. In particular, it was found that the laminar flow is absolutely stable for sufficiently low Reynolds number or sufficiently large suction, while the laminar flow is linearly unstable at high Reynolds number with small suction. Utilizing the LSA, a critical Reynolds number of $\mathrm{Re} \approx 700\,000$ was determined for a crossflow to

top plate speed ratio of $O(1 \times 10^{-5})$. It should be noted that this critical Reynolds number is a first estimate to our findings. Nonetheless, there are notable distinctions between our work and [14]. First, we present a comprehensive analysis of the transition from the PCFT at low transpiration rate to one at very high wall transpiration which corresponds to the ASBL. Second, we improve the precision of critical-Reynolds-number determination and eliminate spurious modes by employing a dispersion relation (DR) derived from the analytical solution of the modified OSE (MOSE), which we discuss in detail in subsequent sections. Later, Ref. [15] extended the work in [14] by investigating the hydrodynamic instability in mutually sliding parallel plates subjected to uniform suction and system rotation. Additionally, a numerical stability analysis of Couette flow over a wavy wall was studied in [16]. Therein it was shown that the presence of wall waviness gives rise to an instability at Re = 5000 that leads to the formation of streamwise vortices. Furthermore, Ref. [17] presented in detail the generation of large-scale streamwise vortices in a laminar PCF with sinusoidal transpiration at the lower wall. Results showed that the threshold amplitude of the transpiration required for the onset of the instability varies approximately as $\mathrm{Re}^{-1.15}$ for large Re. In a more recent study of the PCF, Ref. [18] analyzed the forces needed to sustain the relative motion of parallel plates with a 2D model. Therein a periodic wall transpiration was introduced at the lower plate to mimic the surface roughness and to determined its impact on the laminar flow. The system equations were solved numerically with Chebyshev expansions for modal functions. A different type of bifurcation of PCF driven by periodic transpiration was shown in that work and the results indicated that judicious selection of spatial transpiration patterns can reduce the flow resistance generated by viscous friction. Reference [19] investigated the linear stability of plane porous Couette flow with a uniform vertical throughflow. Therein the Brinkman-extended Darcy equation was used to describe the flow in the porous layer and the equivalent of the Orr-Sommerfeld eigenvalue problem (EVP) was solved numerically using a Chebyshev collocation method. That work presented the neutral stability of PCF in a porous medium for different values of parameters. Additionally, it was found that the presence of throughflow modifies the basic solution and it yields a change in the formulation of the EVP for the analysis of stability of PCF in a porous medium.

Furthermore, many numerical computations have been employed for PCF. Direct numerical simulations (DNSs) of PCF (see Ref. [20]) found that turbulent spots can be sustained for Reynolds numbers above Re = 375 and that the horizontal extent of the spot has an elliptical character, with an aspect ratio that increases with increasing Reynolds number. Reference [21] employed DNS of a highly constrained PCF to investigate the dynamics of the structures found in the near-wall region of turbulent flows. The results therein demonstrated that turbulent PCF could not be maintained below Re = 300. Recently, PCF with constant suction and blowing was first investigated using DNS in [22], discovering that turbulent intensities were observed to decrease with increasing transpiration rate. Further, it was observed that the long and wide characteristic stationary rolls of classical turbulent Couette flow are moved towards the suction wall due to the existence of the wall transpiration.

We are unaware of a LSA of a PCFT. This flow is interesting because it unifies in a finite domain the effect of blowing and suction, and *a priori* the combined effect and its influence on the stability of the flow are largely unknown. For this, the present paper addresses the LSA of PCFT. The organization of the paper is as follows. The stability problem of PCFT is formulated in Sec. II. A transition from PCFT to the ASBL in the large-Re_V limit is introduced in Sec. III. We briefly discuss the numerical methods used in the present study and results in both the temporal and spatial framework in Sec. IV. A summary and conclusions are given in Sec. V.

II. FORMULATION OF THE STABILITY PROBLEM

We consider a PCFT bounded by two walls extending to $\pm\infty$ in the x direction at $y = 0$ and 1. Figure 1 shows that the upper plate is moving relative to the static lower plate at a constant wall velocity U_w. In addition, there is blowing on the lower plate and suction on the upper plate with a uniform transpiration velocity V_0. Due to the independent wall transpiration V_0, two relevant
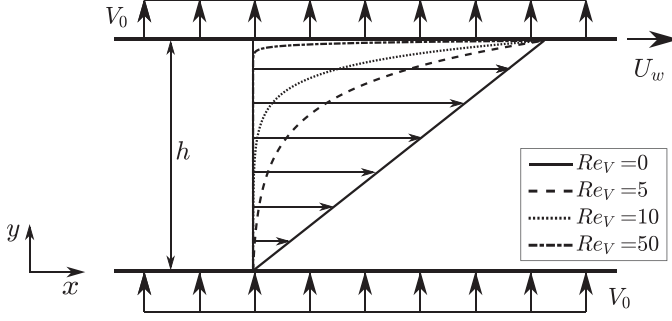
FIG. 1. Dimensionless velocity profile of PCFT with wall-transpiration rates from $\mathrm{Re}_V = 0$ (pure PCF) to $\mathrm{Re}_V = 50$.

Reynolds number are defined as

$$\mathrm{Re} = \frac{U_w h}{\nu}, \quad \mathrm{Re}_V = \frac{V_0 h}{\nu}, \tag{1}$$

where the flow Reynolds number Re is based on the wall velocity U_w and the channel height h and Re_V denotes the transpiration Reynolds number based on the transpiration velocity V_0. The dimensionless base flow of PCFT has the form

$$U(y) = \frac{\mathrm{e}^{\mathrm{Re}_V y} - 1}{\mathrm{e}^{\mathrm{Re}_V} - 1}, \quad V(y) = \frac{\mathrm{Re}_V}{\mathrm{Re}}, \tag{2}$$

where space and velocities have been nondimensionalized by h and U_w. Dimensionless velocity profiles at different Re_V are shown in Fig. 1. It is evident from Fig. 1 that a boundary-layer effect is noticed for increasingly large Re_V and the flow approaches the ASBL. This boundary-layer effect becomes important when choosing the number and distribution of the collocation points for the Chebyshev-collocation method employed in Sec. IV.

The starting point for the subsequent LSA is the MOSE with the laminar base flow velocity $\boldsymbol{U}(y) = (U(y), V(y))^T$ defined in Eq. (2), where the two-dimensional normal-mode ansatz has been applied using the stream-function formulation for the velocity fluctuations (u', v'),

$$\Psi(t, x, y) = \Phi(y)\mathrm{e}^{\mathrm{i}(\alpha x - \omega t)}. \tag{3}$$

Here α denotes the streamwise wave number, ω stands for the frequency, and $\Phi(y)$ denotes the amplitude of the stream function $\Psi(t, x, y)$, which is defined as $u'(y) = \frac{\partial \Psi}{\partial y}$ and $v'(y) = -\frac{\partial \Psi}{\partial x}$. With this the MOSE reads

$$\left[\left(-\mathrm{i}\omega + \mathrm{i}\alpha U(y) + \frac{\mathrm{Re}_V}{\mathrm{Re}}\mathcal{D} \right)(\mathcal{D}^2 - \alpha^2) - \mathrm{i}\alpha\mathcal{D}^2 U(y) - \frac{1}{\mathrm{Re}}(\mathcal{D}^2 - \alpha^2)^2 \right]\Phi(y) = 0, \tag{4}$$

with $\mathcal{D}$ denoting derivatives with respect to y. For this fourth-order ordinary differential equation of the stream function, the corresponding four boundary conditions (BCs) at the two walls are given as

$$\Phi(y = 0) = 0, \quad \Phi(y = 1) = 0,$$
$$\mathcal{D}\Phi|_{y=0} = 0, \quad \mathcal{D}\Phi|_{y=1} = 0. \tag{5}$$

Compared to the classical OSE, the modified Eq. (4) is extended by a first- and a third-order derivative term, scaling with $\mathrm{Re}_V/\mathrm{Re}$ after nondimensionalization, which arises from the constant wall transpiration. It is interesting to note that Eq. (4) admits an exact analytical solution in terms of generalized hypergeometric functions, which was first derived in [23] in the context of the ASBL.

For the present case it reads

$$\Phi(y) = C_1 e^{\alpha y}{}_2F_3\begin{pmatrix} \boldsymbol{a_1} \\ \boldsymbol{b_1} \end{pmatrix}; z(y) + C_2 e^{-\alpha y}{}_2F_3\begin{pmatrix} \boldsymbol{a_2} \\ \boldsymbol{b_2} \end{pmatrix}; z(y) + C_3 e^{\mathrm{Re}_V[(1-\sigma)/2]y}{}_2F_3\begin{pmatrix} \boldsymbol{a_3} \\ \boldsymbol{b_3} \end{pmatrix}; z(y)$$
$$+ C_4 e^{\mathrm{Re}_V[(1+\sigma)/2]y}{}_2F_3\begin{pmatrix} \boldsymbol{a_4} \\ \boldsymbol{b_4} \end{pmatrix}; z(y),$$

(6)

where the parameter σ and the argument $z(y)$ are defined as

$$\sigma = \frac{\sqrt{(\mathrm{Re}_V^2 + 4\alpha^2)(e^{\mathrm{Re}_V} - 1) + 4i(-\alpha + \omega - \omega e^{\mathrm{Re}_V})\mathrm{Re}}}{\mathrm{Re}_V\sqrt{e^{\mathrm{Re}_V} - 1}},$$

$$z(y) = \frac{i\alpha\,\mathrm{Re}\,e^{\mathrm{Re}_V y}}{\mathrm{Re}_V^2(e^{\mathrm{Re}_V} - 1)}.$$

The four linearly independent solutions of Eq. (4) contain the generalized hypergeometric functions ${}_2F_3$ with the vector parameters $\boldsymbol{a_i}$ and $\boldsymbol{b_i}$ defined as

$$\boldsymbol{a_1} = \begin{bmatrix} -\hat{k} + k \\ \hat{k} + k \end{bmatrix}, \quad \boldsymbol{a_2} = \begin{bmatrix} -\hat{k} - k \\ \hat{k} - k \end{bmatrix}, \quad \boldsymbol{a_3} = \begin{bmatrix} \frac{1-\sigma}{2} - \hat{k} \\ \frac{1-\sigma}{2} + \hat{k} \end{bmatrix},$$

$$\boldsymbol{a_4} = \begin{bmatrix} \frac{1+\sigma}{2} + \hat{k} \\ \frac{1+\sigma}{2} - \hat{k} \end{bmatrix}; \quad \boldsymbol{b_1} = \begin{bmatrix} 1 + 2k \\ \frac{1+2k+\sigma}{2} \\ \frac{1+2k-\sigma}{2} \end{bmatrix}, \quad \boldsymbol{b_2} = \begin{bmatrix} 1 - 2k \\ \frac{1-2k-\sigma}{2} \\ \frac{1-2k+\sigma}{2} \end{bmatrix},$$

$$\boldsymbol{b_3} = \begin{bmatrix} 1 - \sigma \\ \frac{3+2k-\sigma}{2} \\ \frac{3-2k-\sigma}{2} \end{bmatrix}, \quad \boldsymbol{b_4} = \begin{bmatrix} 1 + \sigma \\ \frac{3+2k+\sigma}{2} \\ \frac{3-2k+\sigma}{2} \end{bmatrix},$$

(7)

where $k = \frac{\alpha}{Re_V}$ and $\hat{k} = \sqrt{k^2 + 1}$. The four BCs (5) in combination with the derivative of the eigenfunction give rise to the homogeneous matrix equation

$$\boldsymbol{A} \cdot \boldsymbol{C} = \boldsymbol{0},$$

(8)

where the A_{ji} are the respective coefficients (see the Appendix) of the constants C_i [see Eq. (6)] due to the four BCs. For a nontrivial solution the determinant of $\boldsymbol{A}$ has to vanish, yielding the DR

$$\det[A(\alpha, \omega, \mathrm{Re}_V, \mathrm{Re})] = 0,$$

(9)

which summarizes the entire above EVP for the PCFT. It should be mentioned that the coefficients A_{34} and A_{44} of C_4 contain the exponential term $e^{\mathrm{Re}_V[(1+\sigma)/2]}$ at the BC $y = 1$, where the exponent is proportional to $O(\sqrt{\mathrm{Re}})$ for large Re. In this limit these two elements would exceed any other elements. Therefore, we divide the column with the coefficients A_{j4} by the factor $e^{\mathrm{Re}_V[(1+\sigma)/2]}$ before the determinant is taken. Both the temporal and spatial problems have been investigated. Because of their obvious equality on the neutral curve, for most of the subsequent results only the temporal case will be considered further in the remainder of this paper, i.e., we have a real wave number $\alpha \in \mathbb{R}$ and a complex frequency $\omega \in \mathbb{C}$.

III. TRANSITION TO THE ASBL IN THE LARGE-Re_V LIMIT

We will show in this section that, in a special limiting case, PCFT includes the case of the ASBL and the former can be transformed into the latter by elementary transformations and a limiting process. Thus, the stability characteristic of the ASBL is contained in the PCFT.

As was elaborated in the context of Fig. 1, the PCFT essentially evolves from a linear shear flow into an exponential flow profile with boundary-layer characteristics developing with increasing
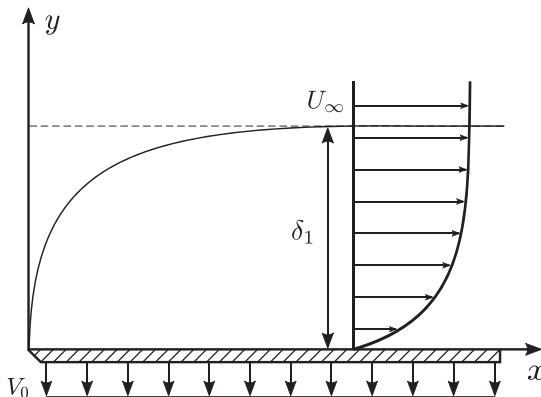
FIG. 2. Dimensionless velocity profile of the ASBL with the displacement thickness δ_1 and wall-normal constant suction V_0.

transpiration rate. Physically speaking, an increasing V_0 leads to flow blockage in the entire bulk and squeezes the flow profile to the upper wall. Although an entirely different flow, the ASBL shares striking similarities with the PCFT, both in the physical manifestation and in the mathematical representation of the solution of the OSE. Each respective laminar base flow features exponential behavior, where the PCFT is defined in Eq. (2) while the ASBL is defined as

$$U(y) = 1 - \mathrm{e}^{-y}, \quad V(y) = -\frac{1}{\widetilde{\mathrm{Re}}}, \tag{10}$$

with $\widetilde{\mathrm{Re}} = \frac{U_\infty}{V_0}$, which is obtained by taking the displacement thickness $\delta_1 = \nu/V_0$ as the length scale.

Upon comparing PCFT at high Re_V and the ASBL, as depicted in Fig. 2, the velocity profiles turn out to be complementary. For PCFT, at the upper wall, where the boundary layer is observed in Fig. 1, the velocity reaches its maximum from where it decays exponentially towards the lower wall. In contrast, the ASBL reaches its minimum at the lower wall and recovers towards the free-stream velocity U_∞ for increasing distances from the wall.

By simple transformations and the limiting case of large Re_V, the two flows can be transformed into each other. What essentially separates both flow profiles is a velocity shift. This discrepancy is resolved by employing the Galilean invariance of Newtonian mechanics, i.e., via adding a negative velocity shift to PCFT of magnitude

$$\Delta U^* = -U_w, \tag{11}$$

in dimensional variables, which after nondimensionalization reads

$$\Delta U = -1. \tag{12}$$

Adding the velocity shift (12) to Eq. (2) gives

$$\tilde{U}(y) = U(y) + \Delta U = \frac{\mathrm{e}^{\mathrm{Re}_V y} - 1}{\mathrm{e}^{\mathrm{Re}_V} - 1} - 1 = \frac{\mathrm{e}^{\mathrm{Re}_V y} - \mathrm{e}^{\mathrm{Re}_V}}{\mathrm{e}^{\mathrm{Re}_V} - 1}. \tag{13}$$

Then the velocity profile of PCFT exposed to Eq. (11) is mirrored around the y axis when compared to the ASBL, as may easily be deduced from Fig. 1. Furthermore, the flow is still locked up by both walls whereas the ASBL is defined on a semi-infinite domain. The latter difference may be accounted for via a coordinate transformation of the form

$$\tilde{y} = (1 - y)\mathrm{Re}_V, \tag{14}$$

where finally $\mathrm{Re}_V \to \infty$ is assumed since the boundary-layer phenomena for PCFT occur for large transpiration rates. A transformation as given in Eq. (14) has two effects. First, the domain is mirrored around the x axis, mapping the upper wall to the lower wall and vice versa. Second, by scaling with Re_V, the formerly lower wall is mapped to infinity, i.e.,

$$y = 0 \Rightarrow \tilde{y} \to \infty, \tag{15a}$$

$$y = 1 \Rightarrow \tilde{y} = 0, \tag{15b}$$

which essentially maps the domain between the two walls to a semi-infinite domain as given for the ASBL. Employing the transformation (14) in Eq. (13) gives

$$\tilde{U}(\tilde{y}) = \frac{\mathrm{e}^{\mathrm{Re}_V}(\mathrm{e}^{-\tilde{y}} - 1)}{\mathrm{e}^{\mathrm{Re}_V} - 1}. \tag{16}$$

The large-Re_V limit then yields

$$\lim_{\mathrm{Re}_V \to \infty} \tilde{U}(\tilde{y}) = \mathrm{e}^{-\tilde{y}} - 1, \tag{17}$$

which equals the profile of the ASBL given in Eq. (10) mirrored around the y axis. This reflection does not change the flow physics of the system.

Simple transformations can be used to transform the PCFT into the ASBL, and we now want to do the same for the stability problem. For this we transform the MOSE for PCFT to the MOSE of the ASBL, which is given by

$$\left[\left(-i\omega + i\alpha U(y) - \frac{1}{\mathrm{Re}} \mathcal{D} \right) (\mathcal{D}^2 - \alpha^2) - i\alpha \mathcal{D}^2 U(y) - \frac{1}{\mathrm{Re}} (\mathcal{D}^2 - \alpha^2)^2 \right] \Phi(y) = 0. \tag{18}$$

They differ in the velocity profiles $U(y)$ as well as in the terms scaling inversely with the Reynolds number Re^{-1}. In fact, as will be demonstrated subsequently, the MOSE of PCFT can be transformed such that the base flow $U(y)$ is replaced by Eq. (17).

For this, first, a transformation of the y coordinate is due to $\mathcal{D}^n = (\mathrm{Re}_V)^n \tilde{\mathcal{D}}^n$, where $\tilde{D}$ is the derivative with respect to $\tilde{y}$. Considering Eq. (4), it becomes apparent that α must also be transformed such that eventually the appearing powers of Re_V due to the transformation of the derivatives may be canceled out globally, i.e.,

$$\alpha = -\mathrm{Re}_V \tilde{\alpha}, \tag{19}$$

where the minus sign is readily explained upon comparing the transformed velocity profile (17), i.e., $\tilde{U}(\tilde{y}) = \mathrm{e}^{-\tilde{y}} - 1$, and the original velocity profile of the ASBL, i.e., $U(y) = 1 - \mathrm{e}^{-y}$. Subsequently, the velocity shift $\Delta U = -1$ is obtained via

$$\omega = \mathrm{Re}_V (\tilde{\omega} - \tilde{\alpha}). \tag{20}$$

This has no influence on the stability characteristic of the flow as real and imaginary values of the PCFT map to real and imaginary values of the ASBL, respectively. One final problem remains, which is the terms scaling with Re^{-1}. These terms will remain with a fourth power of Re_V, while all other terms will scale with a third power of Re_V. This problem is rectified by comparing the definitions of the Reynolds numbers for PCFT and the ASBL, i.e., Eqs. (1) and (10). If we now assume that $U_w = U_\infty$, we observe that the ratios of the Reynolds numbers of Re and Re_V of the PCFT reduce to the one of the ASBL, i.e.,

$$\widetilde{\mathrm{Re}} := \frac{\mathrm{Re}}{\mathrm{Re}_V} = \frac{U_\infty}{V_0}. \tag{21}$$

With this, all necessary transformations are established. Employing all quantities with a tilde into the MOSE (4) for PCFT gives an equation that is mathematically equivalent to the MOSE of the

ASBL given by Eq. (18) in the limit $\mathrm{Re}_V \to \infty$. The four BCs (5) after transformation are finally given by

$$\Phi(y=0) = 0 \Rightarrow \Phi(\tilde{y}=\mathrm{Re}_V) = 0, \tag{22a}$$

$$\Phi(y=1) = 0 \Rightarrow \Phi(\tilde{y}=0) = 0, \tag{22b}$$

$$\mathcal{D}\Phi|_{y=0} = 0 \Rightarrow \tilde{\mathcal{D}}\Phi|_{\tilde{y}=\mathrm{Re}_V} = 0, \tag{22c}$$

$$\mathcal{D}\Phi|_{y=1} = 0 \Rightarrow \tilde{\mathcal{D}}\Phi|_{\tilde{y}=0} = 0, \tag{22d}$$

where we recall again that we have used $\mathrm{Re}_V \to \infty$, which completes the boundary-value problem. Thus, we have formally proven that the ASBL is a special case of PCFT. For the LSA of the ASBL we refer to [8]. One therefore saves the effort of examining PCFT for large Re_V in terms of the rather intricate solutions of Eq. (4). Moreover, we observed a steep rise of computation time when solving for eigenvalues at large Re_V and thus obtaining solutions via the ASBL is evidently more economic.

IV. STABILITY CHARACTERISTICS OF PCFT

A. Numerical methods

In this study, we use two numerical methods to find the eigenvalues of the system consisting of Eqs. (4) and (5) for PCFT. In the first method, subsequently called the local method, the DR (9) is solved for ω using an iterative numerical scheme. The key advantage is that eigenvalues can be computed at arbitrary precision and no spurious modes are generated. For this, the DR (9) is numerically solved using MATLAB with a nonlinear complex root finder based on the CXROOT package in [24], which is based on LMFNLSQ in [25], i.e., an iterative Levenberg-Marquardt algorithm. However, the successful computation of each specific eigenvalue using the local method highly depends on the starting values. Furthermore, the evaluation of the generalized hypergeometric functions is computationally slow. Therefore, this method is used mainly to increase the precision of the results obtained from the collocation method to be described below and to eliminate all spurious modes.

The spectral collocation method is the second computational scheme, in the following called the Chebyshev-Gauss-Lobatto (CGL) method, and is based on Chebyshev polynomials which are applied to Eqs. (4) and (5), which transfers it to a matrix EVP. In turn, this is substituted into a matrix eigenvalue solver, which results in discrete eigenvalue spectra. The collocation scheme is classical, well established for this model class, so for details only we refer the reader to [26]. Although the CGL method can directly provide a large number of eigenvalues, spurious unphysical modes may appear. These eigenvalues are filtered out by employing all eigenvalues from the CGL method as initial guesses in the computation of the eigenvalue based on the local method. With this combination of the local and CGL methods, both an arbitrary precision is achieved and all spurious modes are eliminated.

B. Neutral stability surfaces, curves, and critical parameters

First, the surface of neutral stability of PCFT is examined. Classically, the neutral curve is given in a Re-α coordinate system, which immediately sets out the critical Reynolds number as the smallest Re on the curve of neutral stability. Due to the additional parameter Re_V in our study, the traditional neutral curve is replaced by a neutral surface. A more comprehensive overview of the temporal stability behavior for the present flow is obtained by means of a 3D plot in Figs. 3(a)–3(c), where the temporal neutral surface ($\omega_i = 0$) is plotted as a function of the flow Reynolds number Re, the transpiration Reynolds number Re_V, and the streamwise wave number α. For a fixed Re_V classical stability curves arise, as they are known, e.g., from boundary-layer flows. However, also varying Re_V, it can be seen in Figs. 3(a) and 3(b) that the interior of this surface corresponds to unstable modes. The shape of the neutral surface in Fig. 3(a) shows that the range of unstable streamwise wave numbers α increases rapidly with an increase of the transpiration
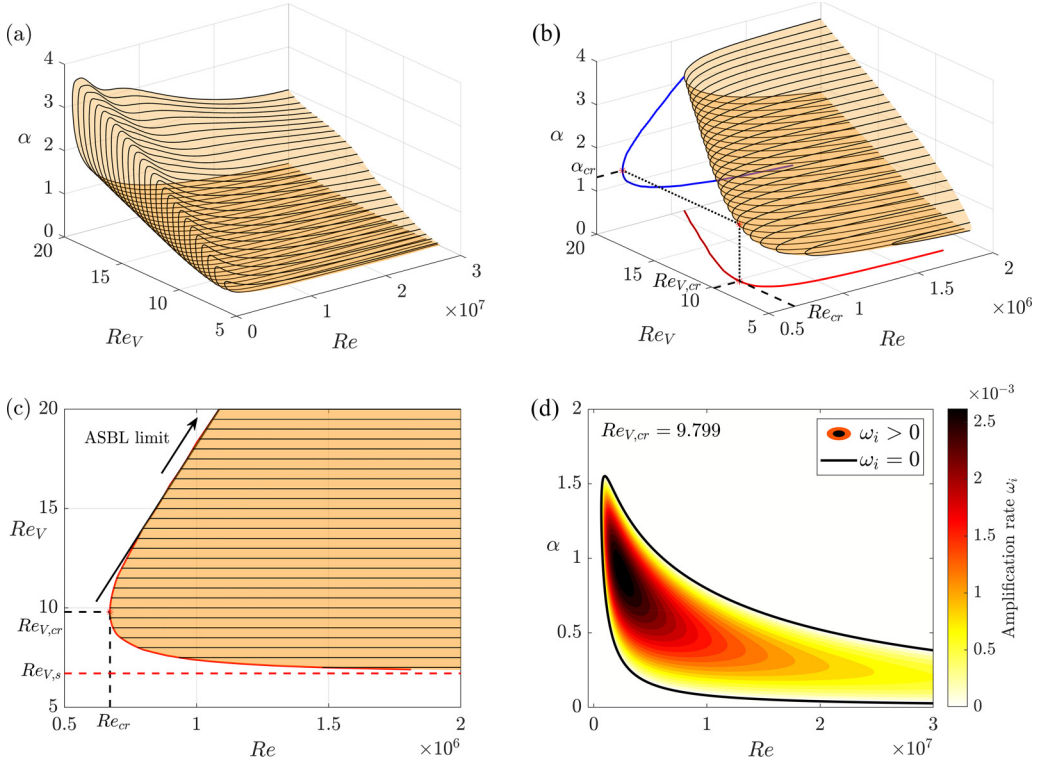
FIG. 3. (a)–(c) Different perspectives, projections, and parameter ranges of the neutral stability surface of PCFT as parametrized by the flow Reynolds number Re, the transpiration Reynolds number Re_V, and the streamwise wave number α. (d) Neutral stability curve at $Re_V = Re_{V,cr}$ together with contours of growth rates $\omega_i > 0$.

Reynolds number Re_V. It is important, however, that the temporal instability may only occur above a distinct threshold for Re_V, as indicated in Fig. 3(c). This threshold of $Re_{V,s} \simeq 6.71$ holds up to very large Re, here tested up to $Re = 3.0 \times 10^7$, and seems to be of universal nature for the entire flow. For small transpiration rates up to the threshold, the PCFT is linearly stable like the PCF without transpiration. For each Re_V above this threshold, a corresponding local critical Reynolds number Re can be identified at which the flow becomes unstable. This parametrization of the local critical Re by Re_V is visualized in a linear scale in Fig. 3(b), or more precisely the projection of the neutral stability surface onto the Re-Re_V plane, which is referred to as the critical curve. This critical curve defines the threshold for the laminar base flow of PCFT required for the onset of temporal instability. From the form of the critical curve it is apparent that there is a particular Re_V where the Reynolds number Re is minimal. This lowest critical Reynolds number at $Re_{cr} = 668\,350.491$ is hereafter called the global critical Reynolds number that entails the global critical transpiration Reynolds number $Re_{V,cr} = 9.799$ and streamwise wave number $\alpha_{cr} = 1.320$. The definition of the global critical parameters was first given in [17]. Beyond this transpiration Reynolds number $Re_{V,cr}$, the local critical Reynolds number Re increases again and continues to grow.

When focusing on $Re_{V,cr}$ the neutral surface reduces to a neutral curve, which is shown in Fig. 3(d). From this it is further observed that the maximum exponential temporal growth rate is $\omega_i = 0.002\,75$ at $Re = 2.4 \times 10^6$ and $\alpha = 0.91$. When further increasing Re, the range of unstable streamwise wave numbers α becomes narrower, while the lower neutral stability branch seems to asymptotically tend towards zero.
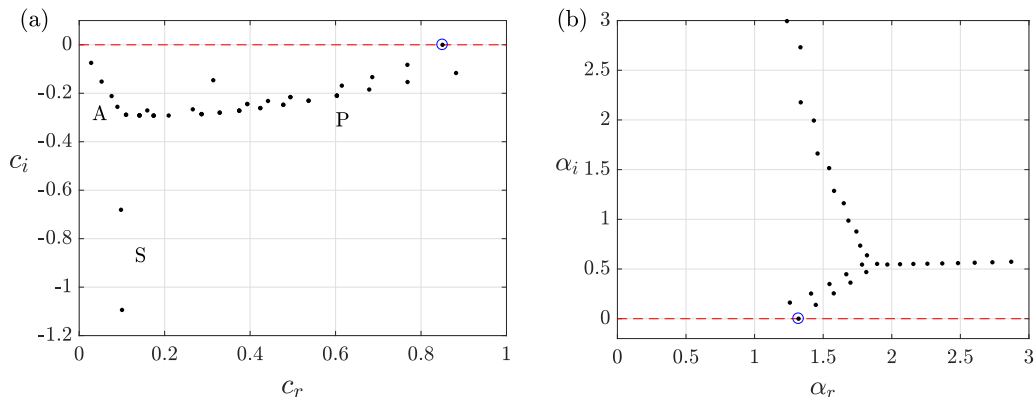
FIG. 4. Temporal and spatial spectra of PCFT at the globally critical values of $\mathrm{Re}_{\mathrm{cr}} = 668\,350.491$ and $\mathrm{Re}_{V,\mathrm{cr}} = 9.799$ for (a) streamwise wave number $\alpha_{\mathrm{cr}} = 1.320$ and (b) frequency $\omega_{\mathrm{cr}} = 1.123$.

The limiting case of the ASBL can be read directly from Fig. 3(c). In the limiting case $\mathrm{Re}_V \to \infty$ the critical curve runs against the linear function between Re_V and Re defined by Eq. (21), i.e., $\mathrm{Re}_V = \mathrm{Re}/\widetilde{\mathrm{Re}}$, and we find that the critical Reynolds number of the ASBL is the inverse of the slope, i.e., $\widetilde{\mathrm{Re}} = 54\,378$, which is exactly the value found in [8].

C. Spectra and eigenfunctions

In the following, starting from the global critical parameters, a closer look is taken at the eigenvalue spectra as well as the eigenfunctions. First, the eigenvalues of the MOSE (4) for PCFT at $\mathrm{Re}_{\mathrm{cr}}$ and $\mathrm{Re}_{V,\mathrm{cr}}$ are shown in Fig. 4. For the actual calculations, we employed $n = 500$ collocation points to calculate the eigenvalues using the CGL method, as mentioned previously, based on a MATLAB Chebyshev collocation code for which the package in [26] was modified. In order to eliminate all spurious modes as well as to increase the accuracy of higher modes in the spectra, all eigenvalues were subsequently iteratively refined by evaluating the DR (9). Concretely, all modes obtained by the spectral collocation method were employed as starting points into the nonlinear root finder for DR (9), which was evaluated with MAPLE 2019 and implemented through Muller's algorithm [27], a second-order secant method. The tolerated residual for the DR (9) was set to a very low threshold, at which the iteration was halted. Due to the highly ill-conditioned behavior of the hypergeometric function for certain parameter ranges, for our iterative refinement it became necessary to set a tolerated residual as low as $O(10^{-100})$ and the number of digits had to be drastically increased to 120 in order to achieve convergence.

For the global critical parameters, Fig. 4(a) displays the temporal eigenvalues c, which are defined as the complex phase velocity with $c = \omega/\alpha$. Branches of eigenvalues for plane Poiseuille flow were classified in [28] as an A branch when $c_r \to 0$, a P branch when $c_r \to 1$, and an S branch when $c_r \to 2/3$, with c_r denoting the real part of the phase velocity.

Analogously, the eigenvalues for PCFT are located on three branches which have been labeled A ($c_r \to 0$), P ($c_r \to 1$), and S ($c_r \approx 0.1$). As indicated in Fig. 4(a), there is one neutrally stable eigenmode on the P branch with $c_i \simeq 0$. The least stable eigenmode corresponds to the Tollmien-Schlichting (TS) wave (see Ref. [29]). The A modes, which tend to have small phase velocities, are designated as lower wall modes, whereas the P modes, which have much higher phase velocities, are referred to as upper wall modes. The S modes for the present flow correspond to a phase speed equal to the average speed of the base flow. This for the PCFT can be calculated from the integral
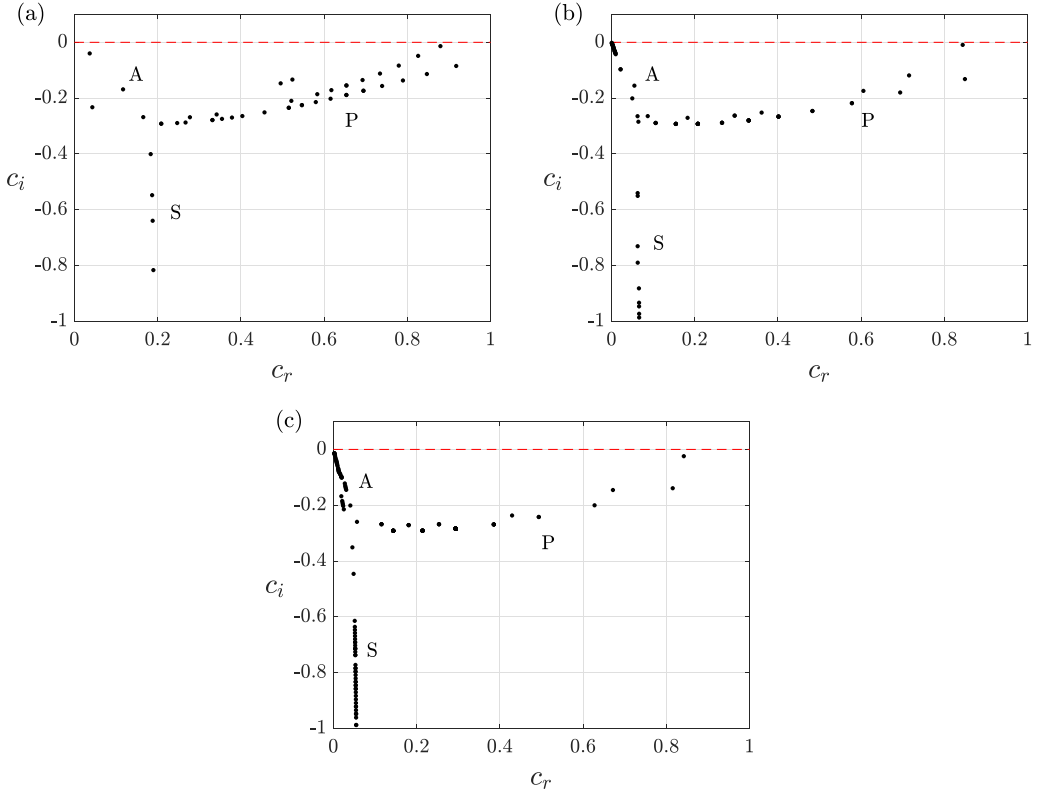
FIG. 5. Temporal spectra are displayed at fixed $\mathrm{Re}_{cr} = 668\,350.491$, $\alpha_{cr} = 1.320$, and varying Re_V for (a) $\mathrm{Re}_V = 5$, (b) $\mathrm{Re}_V = 15$, and (c) $\mathrm{Re}_V = 20$.

of the dimensionless base flow (2) from $y = 0$ to $y = 1$, i.e.,

$$U_m(\mathrm{Re}_V) = \int_0^1 \frac{e^{\mathrm{Re}_V y} - 1}{e^{\mathrm{Re}_V} - 1} dy = \frac{1}{\mathrm{Re}_V} - \frac{1}{e^{\mathrm{Re}_V} - 1}. \tag{23}$$

For the critical value $\mathrm{Re}_{V,cr} = 9.799$ we obtain $U_m = 0.102$, which is close to $c_r = 0.1$ of the S modes in Fig. 4(a). It is evident that the S modes in our present study depend only on the transpiration Reynolds number Re_V. Figure 4(b) shows the spatial spectrum for the global critical parameters. Similar to the temporal case, the spatial spectrum also has three branches, and we again observe the emergence of a neutrally stable eigenvalue with $\alpha_i \simeq 0$, which corresponds to the TS mode.

To understand the effect of variation of Re_V on the temporal eigenvalue spectrum $c = c(\mathrm{Re}, \mathrm{Re}_V, \alpha)$, three more cases are examined. In Fig. 5, the eigenspectra in Re_{cr} and α_{cr} are compared for varying Re_V. The spectra for varying Re_V have similar three-branch structures. The modes on the S branches move with increasing Re_V in the direction of a lower real part of the phase velocity c_r, which is due to the decrease in the bulk velocity of the base flow U_m with increasing Re_V. In addition, we observe that the number of modes on A branches increases and the modes seem to asymptotically tend towards the origin. This may be attributed to the fact that the base flow of PCFT in the vicinity of the lower plate decreases with increasing Re_V and approaches zero with larger Re_V (see Fig. 1). The P branches of spectra have a bifurcated structure and the least stable modes appear on them. When $\mathrm{Re}_V > \mathrm{Re}_{V,cr}$, the imaginary part of the phase velocity c_i of the least stable mode is reduced with increasing Re_V from $c_i = -0.008\,93$ at $\mathrm{Re}_V = 15$ in Fig. 5(b) to $c_i = -0.024\,19$ at $\mathrm{Re}_V = 20$ in Fig. 5(c), i.e., the flow becomes more stable.
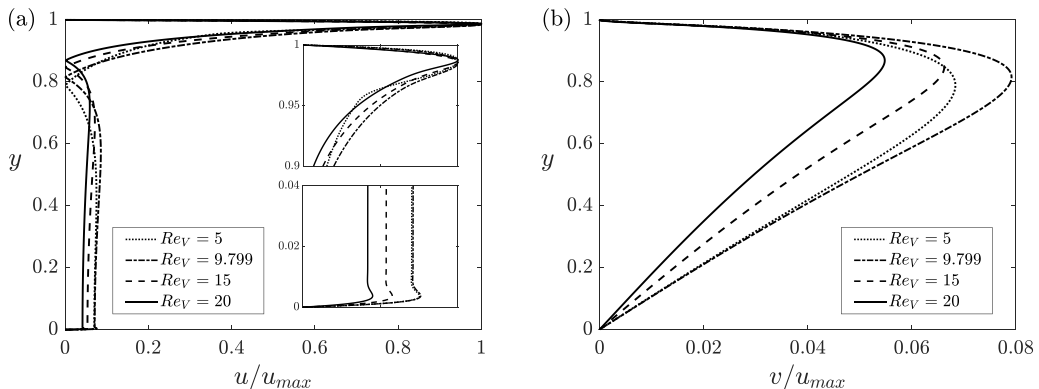
FIG. 6. Plots of the (a) u and (b) v eigenfunctions parametrized by Re_V at fixed $\mathrm{Re} = \mathrm{Re}_{\mathrm{cr}}$ and $\alpha = \alpha_{\mathrm{cr}}$. The eigenfunctions are respectively normalized by the maxima of the u components and were plotted employing the exact solution (6).

Figure 6 displays the eigenfunctions associated with the least stable modes of the spectra in Fig. 5 and the TS mode of the spectrum in Fig. 4(a). The magnitude of the streamwise component u and the wall-normal component v are plotted using the exact eigenfunctions given by Eq. (6). Because of apparent reasons as pointed out in Sec. III, the eigenfunction profiles of the PCFT are similar to those of the ASBL in [7] (see Fig. 4 therein) if mirrored around the y axis compared to the ASBL eigenfunctions. Both velocity eigenfunctions of the PCFT vanish at the lower and upper plates due to their respective boundary conditions. From the shapes of the u eigenfunctions in Fig. 6(a) we observe that the maxima of the eigenfunctions occur close to the upper wall. Boundary-layer-type effects of the u eigenfunction are observed near both the upper and the lower plates with only a weak dependence on Re_v [see insets in Fig. 6(a)]. In addition, Fig. 6(b) shows that the ratio between the v eigenfunctions is larger than for the u eigenfunctions at varying Re_v though their magnitudes are one order of magnitude apart. The stronger v dependence on Re_v might indicate a dominant influence on the stability of the flow.

V. CONCLUSION

The analytical solution of the MOSE (4) for the PCFT based on an exponential velocity profile was derived in terms of $_2F_3$ generalized hypergeometric functions. Together with the boundary conditions at the upper and lower plate, this yielded an EVP which in turn was rewritten into a DR for the complex frequency ω for the temporal problem depending on Re, Re_V, and α. In addition, we showed that in the limiting case $\mathrm{Re}_V \to \infty$, the stability problem for the ASBL is obtained. The EVPs of the PCFT in our study were tackled using two numerical methods, i.e., a local and a CGL method. In the first step in the CGL method the EVP for the stability analysis was solved numerically using the Chebyshev collocation method. In the second step, with the local method based on the DR (9), we inserted all eigenvalues from the collocation method as initial guesses into the DR and as a result were able to (i) eliminate all spurious modes and (ii) at the same time arbitrarily increase the precision of the eigenvalues.

Results of the stability analysis showed that the PCFT is always stable for values of the transpiration Reynolds number below the threshold $\mathrm{Re}_V \leqslant \mathrm{Re}_{V,s} = 6.71$. Beyond this value the flow may become unstable depending on α and Re. Neutral stability surfaces were derived to represent the range of transpiration Reynolds number Re_V and the range of Reynolds number Re for which instability occurs. Furthermore, critical curves were obtained by the projection of the neutral stability surface onto the Re-Re_V plane. On the critical curve a particular point of Re_V was extracted at which the Reynolds number Re is minimal. The globally critical values were determined to $\mathrm{Re}_{\mathrm{cr}} = 668\,350.491$, $\mathrm{Re}_{V,\mathrm{cr}} = 9.799$, $\alpha_{\mathrm{cr}} = 1.320$, and $\omega_{\mathrm{cr}} = 1.123$. Moreover, temporal and spatial

spectra of the PCFT showed that the eigenvalues are located on three branches. In the temporal spectra in Re_{cr} and α_{cr}, by increasing Re_V, the S modes move towards a lower phase velocity due to a decrease in the corresponding averaged speed of the base flow and A modes tend towards the origin, which may be caused by a decline in the base flow near the lower wall. It can further be observed that the TS modes, defined as the most critical mode in the respective spectra, exclusively appear on the P branch, which is in contrast to plane Poiseuille flow, where the critical modes instead appear on the A branch. Finally, the u eigenfunctions develop a strong boundary-layer-like velocity profile near the upper wall. In addition, the ratio between the v and u components reaches its maximum when the flow is neutrally stable.

Note that we intended to refrain from extending the present work further, e.g., to transient growth (TG), instead focusing here on the base modes. To this end, we highlight the two limiting cases of PCFT, i.e., pure PCF without wall transpiration and the ASBL, which represents the limiting case for very high transpiration rates.

Even the case of pure PCF without wall transpiration does not appear to be fully understood to date and, in particular, the theory of TG does not fully describe the transition mechanism (see Refs. [30,31]). Rather, the work of [31] showed very clearly that considering only the linear TG is not sufficient to predict streak instability. It was shown that nonlinear modifications of the TG process must be included in order to assess the instability of the flow. The work of [31,32] then performed and extended a secondary stability analysis of the linear TG in pure PCF. Significantly different methods are required for the pure PCF in order to represent its instability mechanisms (see, e.g., [32–36]).

For the other limiting case of very high transpiration rates, i.e., $Re_V \rightarrow \infty$, it was shown herein that this corresponds to the ASBL. There are a number of theoretical, numerical, and experimental works for the ASBL and they all agree that the critical Reynolds number assumes a very high value, about $Re_{crit} \approx 54\,378$. Care should be taken because the above Reynolds number for the ASBL in the present work is obtained from the ratio of Re/Re_V defined by Eq. (21), and the critical Reynolds number of the ASBL can be read directly from the reciprocal of the slope of the neutral stability curve in the Re-Re_V plane.

The data that support the findings of this study are openly available in [37].

ACKNOWLEDGMENTS

APPENDIX: MATRIX ELEMENTS OF THE COEFFICIENT MATRIX A

With the BCs (5) the matrix elements of the coefficient matrix A in Eq. (8) are given by the expressions

$$\Phi(y=0) = C_1 \underbrace{{}_2F_3\binom{\boldsymbol{a_1}}{\boldsymbol{b_1}}; z(0)}_{A_{11}(\alpha,\omega,Re_V,Re)} + C_2 \underbrace{{}_2F_3\binom{\boldsymbol{a_2}}{\boldsymbol{b_2}}; z(0)}_{A_{12}(\alpha,\omega,Re_V,Re)} + C_3 \underbrace{{}_2F_3\binom{\boldsymbol{a_3}}{\boldsymbol{b_3}}; z(0)}_{A_{13}(\alpha,\omega,Re_V,Re)} + C_4 \underbrace{{}_2F_3\binom{\boldsymbol{a_4}}{\boldsymbol{b_4}}; z(0)}_{A_{14}(\alpha,\omega,Re_V,Re)} = 0,$$

$$\frac{d\Phi(y)}{dy}\bigg|_{y=0} = C_1 \underbrace{\left[\alpha \, {}_2F_3\binom{\boldsymbol{a_1}}{\boldsymbol{b_1}}; z(0) + Re_V z(0)\frac{\overline{a}_1}{\overline{b}_1} {}_2F_3\binom{\boldsymbol{a_1}+\boldsymbol{1}}{\boldsymbol{b_1}+\boldsymbol{1}}; z(0) \right]}_{A_{21}(\alpha,\omega,Re_V,Re)}$$

$$+ C_2 \underbrace{\left[-\alpha \, {}_2F_3\binom{\boldsymbol{a_2}}{\boldsymbol{b_2}}; z(0) + Re_V z(0)\frac{\overline{\overline{a}}_2}{\overline{\overline{b}}_2} {}_2F_3\binom{\boldsymbol{a_2}+\boldsymbol{1}}{\boldsymbol{b_2}+\boldsymbol{1}}; z(0) \right]}_{A_{22}(\alpha,\omega,Re_V,Re)}$$

(A1)

$$+ C_3 Re_V \underbrace{\left[\frac{1-\sigma}{2} {}_2F_3 \begin{pmatrix} \boldsymbol{a_3} \\ \boldsymbol{b_3} \end{pmatrix}; z(0) \right) + z(0) \frac{\overline{a}_3}{\overline{b}_3} {}_2F_3 \begin{pmatrix} \boldsymbol{a_3+1} \\ \boldsymbol{b_3+1} \end{pmatrix}; z(0) \right)\right]}_{A_{23}(\alpha,\omega,Re_V,Re)}$$

$$+ C_4 Re_V \underbrace{\left[\frac{1+\sigma}{2} {}_2F_3 \begin{pmatrix} \boldsymbol{a_4} \\ \boldsymbol{b_4} \end{pmatrix}; z(0) \right) + z(0) \frac{\overline{a}_4}{\overline{b}_4} {}_2F_3 \begin{pmatrix} \boldsymbol{a_4+1} \\ \boldsymbol{b_4+1} \end{pmatrix}; z(0) \right)\right]}_{A_{24}(\alpha,\omega,Re_V,Re)} = 0, \quad (A2)$$

$$\Phi(y=1) = C_1 \underbrace{e^\alpha {}_2F_3 \begin{pmatrix} \boldsymbol{a_1} \\ \boldsymbol{b_1} \end{pmatrix}; z(1) \right)}_{A_{31}(\alpha,\omega,Re_V,Re)} + C_2 \underbrace{e^{-\alpha} {}_2F_3 \begin{pmatrix} \boldsymbol{a_2} \\ \boldsymbol{b_2} \end{pmatrix}; z(1) \right)}_{A_{32}(\alpha,\omega,Re_V,Re)} + C_3 \underbrace{e^{Re_V[(1-\sigma/)2]} {}_2F_3 \begin{pmatrix} \boldsymbol{a_3} \\ \boldsymbol{b_3} \end{pmatrix}; z(1) \right)}_{A_{33}(\alpha,\omega,Re_V,Re)}$$

$$+ C_4 \underbrace{e^{Re_V[(1+\sigma/)2]} {}_2F_3 \begin{pmatrix} \boldsymbol{a_4} \\ \boldsymbol{b_4} \end{pmatrix}; z(1) \right)}_{A_{34}(\alpha,\omega,Re_V,Re)} = 0, \quad (A3)$$

$$\frac{d\Phi(y)}{dy}\bigg|_{y=1} = C_1 \underbrace{e^\alpha \left[\alpha \, {}_2F_3 \begin{pmatrix} \boldsymbol{a_1} \\ \boldsymbol{b_1} \end{pmatrix}; z(1) \right) + Re_V z(1) \frac{\overline{a}_1}{\overline{b}_1} {}_2F_3 \begin{pmatrix} \boldsymbol{a_1+1} \\ \boldsymbol{b_1+1} \end{pmatrix}; z(1) \right) \right]}_{A_{41}(\alpha,\omega,Re_V,Re)}$$

$$+ C_2 \underbrace{e^{-\alpha} \left[-\alpha \, {}_2F_3 \begin{pmatrix} \boldsymbol{a_2} \\ \boldsymbol{b_2} \end{pmatrix}; z(1) \right) + Re_V z(1) \frac{\overline{a}_2}{\overline{b}_2} {}_2F_3 \begin{pmatrix} \boldsymbol{a_2+1} \\ \boldsymbol{b_2+1} \end{pmatrix}; z(1) \right) \right]}_{A_{42}(\alpha,\omega,Re_V,Re)}$$

$$+ C_3 Re_V \underbrace{e^{Re_V[(1-\sigma)/2]} \left[\frac{1-\sigma}{2} {}_2F_3 \begin{pmatrix} \boldsymbol{a_3} \\ \boldsymbol{b_3} \end{pmatrix}; z(1) \right) + z(1) \frac{\overline{a}_3}{\overline{b}_3} {}_2F_3 \begin{pmatrix} \boldsymbol{a_3+1} \\ \boldsymbol{b_3+1} \end{pmatrix}; z(1) \right) \right]}_{A_{43}(\alpha,\omega,Re_V,Re)}$$

$$+ C_4 Re_V \underbrace{e^{Re_V[(1+\sigma)/2]} \left[\frac{1+\sigma}{2} {}_2F_3 \begin{pmatrix} \boldsymbol{a_4} \\ \boldsymbol{b_4} \end{pmatrix}; z(1) \right) + z(1) \frac{\overline{a}_4}{\overline{b}_4} {}_2F_3 \begin{pmatrix} \boldsymbol{a_4+1} \\ \boldsymbol{b_4+1} \end{pmatrix}; z(1) \right) \right]}_{A_{44}(\alpha,\omega,Re_V,Re)} = 0,$$

$$(A4)$$

where $\frac{\overline{a}_i}{\overline{b}_i} = \frac{a_{i1} a_{i2}}{b_{i1} b_{i2} b_{i3}}$ and we have further made use of the identity $\frac{d}{dy} {}_2F_3 \begin{pmatrix} \boldsymbol{a} \\ \boldsymbol{b} \end{pmatrix}; y) = {}_2F_3 \begin{pmatrix} \boldsymbol{a+1} \\ \boldsymbol{b+1} \end{pmatrix}; y)$.

---

[1] W. Pfenninger, Untersuchungen über reibungsverminderungen an tragflügeln: Insbesondere mit hilfe von grenzschichtabsaugung, Ph.D. thesis, ETH Zurich, 1946.

[2] A. L. Braslow, D. L. Burrows, N. Tetervin, and F. Visconti, Experimental and theoretical studies of area suction for the control of the laminar boundary layer on an NACA 64a010 airfoil, NASA Report No. NACA-TR-1025 (NASA, 1951), https://ntrs.nasa.gov/citations/19930092080.

[3] J. Pretsch, Umschlagbeginn und Absaugung: Ein Beitrag der Grenzschichttheorie, Tech. Rep. AVA-42/F/02 (Aerodynamische Versuchsanstalt Göttingen, 1942), https://elib.dlr.de/83188/.

[4] P. Chiarulli and J. C. Freeman, *Stability of the Boundary Layer* (Air Material Command, Wright-Patterson AFB, 1948), Vol. 6.

[5] T. Hughes and W. Reid, On the stability of the asymptotic suction boundary-layer profile, J. Fluid Mech. **23**, 715 (1965).

[6] L. Hocking, Non-linear instability of the asymptotic suction velocity profile, Q. J. Mech. Appl. Math. **28**, 341 (1975).

[7] J. H. Fransson and P. Alfredsson, On the disturbance growth in an asymptotic suction boundary layer, J. Fluid Mech. **482**, 51 (2003).

[8] A. Yalcin, Y. Turkac, and M. Oberlack, On the temporal linear stability of the asymptotic suction boundary layer, Phys. Fluids **33**, 054111 (2021).

[9] D. M. Sheppard, Hydrodynamic stability of the flow between parallel porous walls, Phys. Fluids **15**, 241 (1972).

[10] V. A. Romanov, Stability of plane-parallel Couette flow, Funct. Anal. Appl. **7**, 137 (1973).

[11] N. Tillmark and P. H. Alfredsson, Experiments on transition in plane Couette flow, J. Fluid Mech. **235**, 89 (1992).

[12] F. Nicoud and J.-R. Angilella, Effects of uniform injection at the wall on the stability of Couette-like flows, Phys. Rev. E **56**, 3000 (1997).

[13] D. Barkley and L. S. Tuckerman, Stability analysis of perturbed plane Couette flow, Phys. Fluids **11**, 1187 (1999).

[14] C. R. Doering, E. A. Spiegel, and R. A. Worthing, Energy dissipation in a shear layer with suction, Phys. Fluids **12**, 1955 (2000).

[15] K. Deguchi, N. Matsubara, and M. Nagata, Suction–shear–coriolis instability in a flow between parallel plates, J. Fluid Mech. **760**, 212 (2014).

[16] J. Floryan, Centrifugal instability of Couette flow over a wavy wall, Phys. Fluids **14**, 312 (2002).

[17] J. Floryan, Wall-transpiration-induced instabilities in plane Couette flow, J. Fluid Mech. **488**, 151 (2003).

[18] L. Jiao and J. M. Floryan, Use of transpiration for reduction of resistance to relative movement of parallel plates, Phys. Rev. Fluids **6**, 014101 (2021).

[19] B. Shankar and I. Shivakumara, Changes in the hydrodynamic stability of plane porous-Couette flow due to vertical throughflow, Phys. Fluids **33**, 074103 (2021).

[20] A. Lundbladh and A. V. Johansson, Direct simulation of turbulent spots in plane Couette flow, J. Fluid Mech. **229**, 499 (1991).

[21] J. M. Hamilton, J. Kim, and F. Waleffe, Regeneration mechanisms of near-wall turbulence structures, J. Fluid Mech. **287**, 317 (1995).

[22] S. Kraheberger, S. Hoyas, and M. Oberlack, DNS of a turbulent Couette flow at constant wall transpiration up to $\mathrm{Re}_\tau = 1000$, J. Fluid Mech. **835**, 421 (2018).

[23] P. Baldwin, The stability of the asymptotic suction boundary layer profile, Mathematika **17**, 206 (1970).

[24] M. Balda, LMFsolve.m: Levenberg-Marquardt-Fletcher algorithm for nonlinear least squares problems (MathWorks, Natick, 2012), file exchange 16063, https://www.mathworks.com/matlabcentral/fileexchange/16063-lmfsolve-m-levenberg-marquardt-fletcher-algorithm-for-nonlinear-least-squares-problems.

[25] R. Fletcher, A modified Marquardt subroutine for nonlinear least squares, AERE Harwell Report R 6799 (Atomic Energy Research Establishment, Harwell, 1971).

[26] P. J. Schmid, D. S. Henningson, and D. Jankowski, Stability and transition in shear flows. Applied mathematical sciences, Vol. 142, Appl. Mech. Rev. **55**, B57 (2002).

[27] D. E. Muller, A method for solving algebraic equations using an automatic computer, Math. Tables Aids Comput. **10**, 208 (1956).

[28] L. M. Mack, A numerical study of the temporal eigenvalue spectrum of the Blasius boundary layer, J. Fluid Mech. **73**, 497 (1976).

[29] W. Tollmien, General instability criterion of laminar velocity distributions, NASA Report No. NACA-TM-792 (NASA, 1936), https://ntrs.nasa.gov/citations/19930094625.

[30] K. M. Butler and B. F. Farrell, Three-dimensional optimal perturbations in viscous shear flow, Phys. Fluids **4**, 1637 (1992).

[31] M. Karp and J. Cohen, Tracking stages of transition in Couette flow analytically, J. Fluid Mech. **748**, 896 (2014).

[32] M. Karp and J. Cohen, On the secondary instabilities of transient growth in Couette flow, J. Fluid Mech. **813**, 528 (2017).

[33] S. C. Reddy, P. J. Schmid, J. S. Baggett, and D. S. Henningson, On stability of streamwise streaks and transition thresholds in plane channel flows, J. Fluid Mech. **365**, 269 (1998).

[34] S. Cherubini and P. De Palma, Nonlinear optimal perturbations in a Couette flow: bursting and transition, J. Fluid Mech. **716**, 251 (2013).

[35] Y. Duguet, A. Monokrousos, L. Brandt, and Dan S. Henningson, Minimal transition thresholds in plane Couette flow, Phys. Fluids **25**, 084103 (2013).

[36] T. Dokoza and M. Oberlack, Reynolds number induced growth of the large-scale rolls in plane Couette flow using resolvent analysis, J. Fluid Mech. **968**, A23 (2023).

[37] W. Sun, A. Yalcin, and M. Oberlack, Stability of plane Couette flow with wall transpiration [Dataset] (2024), https://doi.org/10.48328/tudatalib-909.